Physical Basis of Large Microtubule Aster Growth

Keisuke Ishihara[1, 2, 3, *], Kirill S. Korolev[4,*], Timothy J. Mitchison[1, 2]

[1] Department of Systems Biology, Harvard Medical School
200 Longwood Avenue, Boston, MA, USA 02115

[2] Cell Division Group, Marine Biological Laboratory
7 MBL Street, Woods Hole, MA, USA 02543

[3] Present address: Center for Systems Biology Dresden
Pfotenhauerstr. 108, Dresden, Germany 01307

[4] Department of Physics and Graduate Program in Bioinformatics
Boston University, Boston, MA, USA 02215

[*] Corresponding authors: ishihara@mpi-cbg.de, korolev@bu.edu

version Sunday 26th June, 2016

Abstract

Microtubule asters - radial arrays of microtubules organized by centrosomes - play a fundamental role in the spatial coordination of animal cells. The standard model of aster growth assumes a fixed number of microtubules originating from the centrosomes. This model does not scale with cell size, and we recently found evidence for microtubule nucleation away from centrosomes. Here, we combine microtubule nucleation and polymerization dynamics to develop a biophysical model of aster growth. Our model predicts that asters expand as traveling waves and recapitulates all major aspects of aster growth. Strikingly, the model predicts an explosive transition from stationary to growing asters with a discontinuous jump of the expansion velocity to a nonzero value. Experiments in frog egg extract confirm main theoretical predictions. Our results suggest that asters are a meshwork of short, shrinking microtubules maintained by autocatalytic nucleation and provide a paradigm for the assembly of robust and evolvable polymer networks.

INTRODUCTION

Animal cells use asters, radial arrays of microtubules, to spatially organize their cytoplasm (Wilson, 1896). Specifically, astral microtubules transport organelles (Grigoriev et al., 2008; Wang et al., 2013; Waterman-Storer and Salmon, 1998), support cell motility by mediating mechanical and biochemical signals (Etienne-Manneville, 2013), and are required for proper positioning of the nucleus, the mitotic spindle, and the cleavage furrow (Field et al., 2015; Grill and Hyman, 2005; Neumüller and Knoblich, 2009; Tanimoto et al., 2016; Wilson, 1896). Individual microtubules undergo dynamic instability (Mitchison and Kirschner, 1984): They either grow (polymerize) or shrink (depolymerize) at their plus ends and occasionally undergo stochastic transition between these two states. Collective behavior of microtubules is less well understood, and it is not clear how dynamic instability of individual microtubules controls aster growth and function.

The standard model of aster growth posits that centrosomes nucleate and anchor all microtubules at their minus ends while the plus ends polymerize outward via dynamic instability (Brinkley, 1985). As a result, aster growth is completely determined by the dynamics of individual microtubules averaged over the growing and shrinking phases. In particular, the aster either expands at a velocity given by the net growth rate of microtubules or remains stationary if microtubules depolymerize on average (Belmont et al., 1990; Dogterom and Leibler, 1993; Verde et al., 1992).

The standard model for aster growth is being increasingly challenged by reports of microtubules with their minus ends located far away from centrosomes (Akhmanova and Steinmetz, 2015; Keating and Borisy, 1999). Some of these microtubules may arise simply by detachment from centrosomes (Keating et al., 1997; Waterman-Storer et al., 2000) or severing of pre-existing microtubules (Roll-Mecak and McNally, 2010). However, new microtubules could also arise due to a nucleation processes independent of centrosomes (Clausen and Ribbeck, 2007; Efimov et al., 2007; Petry et al., 2013) and contribute to both aster growth and its mechanical properties. We recently challenged the standard model as an explanation of large asters in early embryo cells because its demands a decrease in microtubule density at the periphery, which is inconsistent with aster morphology in frog and fish embryos (Wühr et al., 2008, 2010). Instead, we

proposed an autocatalytic nucleation model, where microtubules or microtubule plus ends stimulate the nucleation of new microtubules at the aster periphery (Ishihara et al., 2014a,b; Wühr et al., 2009). This mechanism generates new microtubules necessary to maintain a constant density as the aster expands. We also hypothesized that autocatalytic nucleation could effectively rectify length fluctuations of individual microtubules, and allow rapid growth of large asters made of short, unstable microtubules. However, we did not provide a quantitative model that can be compared to the experiments or even show that the proposed mechanism is feasible.

Here, we develop a quantitative biophysical model of aster growth with autocatalytic nucleation. It predicts that asters can indeed expand even when individual microtubules depolymerize (shrink) on average. In this regime, aster expansion is driven by the increase in the total number of microtubules, and the resulting aster is a network of short interconnected microtubules. The transition from stationary to growing asters depends on the balance between polymerization dynamics and nucleation. At this transition, our theory predicts a minimum rate at which asters grow, which we define as the gap velocity. This gap velocity arises due to the dynamic instability of microtubule polymerization and excludes a wide class of alternative models. More importantly, this mode of aster growth allows the cell to assemble asters with varying polymer densities at consistently large speeds. Using a cell-free reconstitution approach (Field et al., 2014; Nguyen et al., 2014), we perform biochemical perturbations and observe the slowing down and eventual arrest of aster growth with a substantial gap velocity at the transition. By combining theory and experiments, we provide a quantitative framework for how the cell cycle may regulate the balance between polymerization dynamics and nucleation to control aster growth. We also propose that the growth of large interphase asters is an emergent property of short microtubules that constantly turnover and self-amplify.

RESULTS

Conceptual Model for Aster Growth based on Polymerization Dynamics and Autocatalytic Nucleation

To describe the polymerization dynamics of plus ends, we adopt the standard two-state model of microtubule dynamic instability (Fig. 1A). In this model, a single microtubule is in one of the two states: (i) the growing state, where plus ends polymerize at rate v_{grow} and (ii) the shrinking state, where plus ends depolymerize at rate v_{shrink}. A growing microtubule may transition to a shrinking state (catastrophe event) with rate f_{cat}. Similarly, the shrinking to growing transition (rescue event) occurs at rate f_{res}. These parameters define the mean elongation rate J given by the time-weighted average of polymerization and depolymerization.

Depending on the sign of J, one distinguishes two regimes of the dynamic instability: bounded ($J < 0$) and unbounded ($J > 0$) (Dogterom and Leibler, 1993; Verde et al., 1992). The change between these regimes was hypothesized to drive the transition from small mitotic asters to large interphase asters because the standard model posits that asters are produced by the expansion of individual microtubules (Fig. 1B left, "individual growth"). In the bounded regime, the standard model predicts a stationary aster assuming that microtubules that shrink all the way to the centrosomes immediately re-nucleate. In the unbounded regime, the standard model predicts an aster that (1) increases its radius at a rate equal to the mean polymerization rate J, (2) consists of a fixed number of microtubules, and (3) contains microtubules as long as the aster radius.

Below, we add autocatalytic microtubule nucleation to the standard model (Fig. 1A) and propose the "collective growth" regime (Fig. 1B, right). Specifically, we assume that new microtubules nucleate at locations away from centrosomes at rate Q, which depends on the local density of growing plus ends, i.e. plus-ends serve as nucleation sites or otherwise catalyze nucleation (other nucleation mechanisms are discussed in SI). The new microtubules have zero length and tend to grow radially due to mechanical interactions with the existing microtubule network. These non-centrosomal microtubules disappear when they shrink back to their minus ends. Our assumptions

are broadly consistent with known microtubule physiology (Clausen and Ribbeck, 2007; Petry et al., 2013), and we found strong evidence for nucleation away from centrosomes in egg extract by microtubule counting in growing asters (Ishihara et al., 2014a).

Without negative feedback, autocatalytic processes lead to exponential growth, but there are several lines of evidence for an apparent carrying capacity of microtubules in a given cytoplasmic volume (Clausen and Ribbeck, 2007; Ishihara et al., 2014a; Petry et al., 2013). Such a limitation is inevitable since the building blocks of microtubules are present at a fixed concentration. In our model, we impose a carrying capacity by expressing autocatalytic nucleation as a logistic function of the local density of growing plus ends, which is qualitatively consistent with local depletion of nucleation factors such as the gamma-tubulin ring complex. Other forms of negative feedback, e.g. at the level of polymerization dynamics, are possible as well. In SI, we show that the type of negative feedback does not affect the rate of aster growth, which is determined entirely by the dynamics at the leading edge of a growing aster where the microtubule density is small and negative feedback can be neglected.

Mathematical Model of Autocatalytic Growth of Asters

Assuming large number of microtubules, we focus on the mean-field or deterministic dynamics (SI) and formalize our model as a set of partial differential equations. Specifically, we let $\rho_g(t,x,l)$ and $\rho_s(t,x,l)$ denote respectively the number of growing and shrinking microtubules of length l with their minus ends at distance $x>0$ from the centrosome. The polymerization dynamics and nucleation are then described by,

$$\begin{cases} \dfrac{\partial \rho_g}{\partial t} = -v_g \dfrac{\partial \rho_g}{\partial l} - f_{cat}\rho_g + f_{res}\rho_s + Q(x)\cdot\delta(l) \\ \dfrac{\partial \rho_s}{\partial t} = +v_s \dfrac{\partial \rho_s}{\partial l} + f_{cat}\rho_g - f_{res}\rho_s \end{cases} \tag{1}$$

Nucleation is represented by the term $Q(x) = rC_g(t,x)(1-C/K)$, where r is the nucleation rate, K is the carrying capacity controlling the maximal microtubule density, and $C_g(t,x)$ is the local density of the growing plus ends at point x. Microtubules of varying length and minus end positions contribute to $C_g(t,x)$, which can be expressed as a convolution of ρ_g (see SI). The delta-function $\delta(l)$ ensures that nucleated microtubules have zero length. Note that polymerization and depolymerization changes

the microtubule length l, but not the minus end position x. Equations at different x are nevertheless coupled due to the nucleation term, which depends on x through C_g.

Asters Grow as Spatially Propagating Waves with Constant Bulk Density

To check if our model can describe aster growth, we solved Eq. (1) numerically using finite difference methods in an 1D planar geometry. With relatively low nucleation rates, microtubule populations reached a steady-state profile confined near the origin reminiscent of an aster in the standard model with bounded microtubule dynamics (Fig. 2A left). When the nucleation rate was increased, the microtubule populations expanded as a travelling wave with an approximately invariant shape (Fig. 2A right) consistent with the growth of interphase asters in our reconstitution experiments (Fig. 2B and (Ishihara et al., 2014a)). Further, these behaviors were observed with experimentally measured parameters (Table 1).

Similar to the behavior of real asters, our model predicted two qualitatively different aster states corresponding to interphase and mitosis: (i) stationary asters with small, constant radii and (ii) growing asters characterized by a linear increase in radius over time and a constant microtubule density at the periphery. The transition between these states was controlled by model parameters suggesting that aster assembly and disassembly during cell cycle can be driven by changes in the kinetics of microtubule nucleation or polymerization.

Analytical Solution for Growth Velocity and Critical Nucleation

We solved Eq. (1) exactly and obtained an analytical expression for the growth rate of an aster in terms of model parameters; the details of the calculation are summarized in SI, and the main conclusions are presented in Fig. 3.

Fig. 3A shows how aster expansion velocity V is affected by the mean polymerization rate J. In the absence of nucleation ($r = 0$), our model reduces to the standard model (Fig. 1A blue line) and predicts that asters only grow when J¿0 with $V = J$. When nucleation is allowed ($r > 0$) (Fig. 1A red line), the growth velocity increases with r and asters can grow even when individual microtubules shrink on

average, i.e. $J < 0$ (Fig. 3A and 3B). In this regime, asters are composed of short microtubules, which constantly depolymerize and re-nucleate. Thus, nucleation enables asters to span length scales far exceeding the length of an individual microtubule. This underscores the contrast with the standard model and shows that nucleation contributes, not only to the increased number of microtubules in the aster, but also to the spatial organization and growth rates of asters.

When $J < 0$, a critical nucleation rate is required for aster growth (Fig. 3B). Indeed, microtubules constantly disappear as their length shrinks to zero, and the nucleation of new microtubules need to occur frequently enough to overcome the microtubule loss. Consistent with this argument, our analytical solution predicts no aster growth below a certain value of nucleation (SI), termed critical nucleation rate r_c:

$$r_c = f_{cat} - \frac{v_g}{v_s} f_{res}. \tag{2}$$

The right hand side of this equation is the inverse of the average time that a microtubule spends in the growing state before shrinking to zero-length and disappearing (SI). Thus, aster growth requires that, on average, a microtubule needs to nucleate at least one new microtubule during its lifetime.

The dependence of the critical nucleation rate on model parameters is very intuitive. Increasing the parameters in favor of polymerization (v_g and f_{res}), lowers the threshold level of nucleation required for aster growth, while increasing the parameters in favor of depolymerization (v_s and f_{cat}), has the opposite effect. We also find that $r_c = 0$ when J $= 0$, suggesting that there is no critical nucleation rate for $J \geq 0$. This limit is consistent with the standard model with $J > 0$ and $r = 0$ where the aster radius increases albeit with radial dilution of microtubule density (Fig. 1B). The critical nucleation rate conveys the main implication of our theory: the balance between polymerization dynamics and autocatalytic nucleation defines the quantitative condition for continuous aster growth.

Explosive Transition to Growth with a Gap Velocity

At the critical nucleation rate, the aster expansion velocity V takes a positive, non-zero value, which we refer to as the "gap velocity" (SI):

$$V_{gap} \equiv \lim_{r \to r_c} V = \frac{-v_g v_s (v_g f_{res} - v_s f_{cat})}{v_g^2 f_{res} + v_s^2 f_{cat}}. \quad (3)$$

This finite jump in the aster velocity as the nucleation rate is increased beyond r_c is a consequence of microtubule dynamic instability and is in sharp contrast to the behavior of reaction-diffusion systems, where travelling fronts typically become infinitesimally slow before ceasing to propagate (Chang and Ferrell, 2013; Hallatschek and Korolev, 2009; Méndez et al., 2007; van Saarloos, 2003). One can understand the origin of $V_{gap} > 0$ when microtubules are eliminated after a catastrophe event ($f_{res} = 0; J = -v_s$). In this limit, plus ends always expand with the velocity v_g both before and after nucleation until they eventually collapse. Below r_c, this forward expansion of plus ends fails to produce aster growth because the number of plus ends declines on average. Right above r_c, the number of plus ends is stable and aster grows at the same velocity as individual microtubules. Indeed, Eq. (3) predicts that $V_{gap} = v_g$ when $f_{res} = 0$. The dynamics are similar for $f_{res} > 0$. At the transition, nucleation stabilizes the number of microtubules expanding forward, and their average velocity sets the value of V_{gap}. We also find that the magnitude of V_{gap} is inversely proportional to the mean length of microtubules in the system (SI). Thus, the shorter the microtubules, the more explosive this transition becomes.

In the SI, we also show that microtubule density inside the aster is proportional to $r - r_c$. Thus, the density is close to zero during the transition from stationary to growing asters, but quickly increases as the nucleation rate becomes larger. As a result, cells can achieve rapid aster growth while keeping the density of the resulting microtubule network sufficiently low. The low density might be beneficial because of its mechanical properties or because it simply requires less tubulin to produce and energy to maintain. In addition, the explosive transition to growth with $V_{gap} > 0$ allows the cell to independently control the aster density and growth speed.

Model parameters other than the nucleation rate can also be tuned to transition asters from growth to no growth regimes. Similar to equations (2) and (3), one can

define the critical parameter value and gap velocity to encompass all such transitions (SI). In all cases, we find that the onset of aster growth is accompanied by discontinuous increase in the growth velocity. Moreover, the transition to growth always occurs at $J < 0$ unless the nucleation rate is exactly zero as in the standard model.

Titration of MCAK Slows then Arrests Aster Growth with Evidence for a Gap Velocity

Based on our theory, we reasoned that it would be possible to transform a growing interphase aster to a small, stationary aster by tuning polymerization dynamics and/or nucleation via biochemical perturbations in *Xenopus* egg extract. To this end, we performed a reconstitution experiment in undiluted interphase cytoplasm supplied with anti-Aurora kinase A antibody coated beads, which nucleate microtubules and initiate aster growth under the coverslip (Field et al., 2014; Ishihara et al., 2014a). We explored perturbation of various dynamics regulators, seeking one whose effect was restricted to influencing a single parameter in our model. This was challenging since proteins that regulate polymerization dynamics tend to also regulate nucleation, and nucleation itself has not been characterized at a molecular level. We settled on perturbation of MCAK/KIF2C, the main catastrophe-promoting factor in the extract system (Kinoshita et al., 2001; Walczak et al., 1996) and performed time-lapse imaging of aster growth.

In control reactions, aster radius, visualized by the plus end marker EB1-mApple, increased at velocities of $20.3 \pm 3.1 \mu m/min$ (n=21 asters). We saw no detectable changes to aster growth with addition of the wild type MCAK protein. In contrast, addition of MCAK-Q710, a mutant construct with enhanced catastrophe-promoting activity (Moore and Wordeman, 2004), decreased aster growth velocity (Fig. 4A and B). At concentrations of MCAK-Q710 above a critical concentration of 320 nM, most asters had small radii with very few microtubules growing from the Aurora A beads. This behavior is consistent with the effects of reducing f_{cat} in our analytical solution although changes in other model parameters such as the nucleation rate could also produce similar results (SI).

At 320nM MCAK-Q710 concentration, we observed bimodal behavior. Some asters increased in radius at moderate rates, while other asters maintained a stable size before

disappearing, presumably due to the decrease of centrosomal nucleation over time (Fig. S2 and (Ishihara et al., 2014a)). In particular, we observed no asters growing at velocities between 0 and $9\mu m/min$ (Fig. 4B and S2). This gap in the range of possible velocities is consistent with the theoretical prediction that growing asters expand above a minimal rate V_{gap}.

To confirm that the failure of aster growth above the critical concentration of MCAK-Q710 is caused by the changes in aster growth rather than aster initiation on the beads, we repeated the experiments with Tetrahymena pellicles as the initiating centers instead of Aurora A beads. Pellicles are pre-loaded with a high density of microtubule nucleating sites, and are capable of assembling large interphase asters (Ishihara et al., 2014a). We found pellicle initiated asters to exhibit a similar critical concentration of MCAK-Q710 compared to Aurora A bead asters (Fig. S3). While the majority of Aurora A beads subjected to the highest concentration of MCAK-Q710 lost growing microtubules over time, a significant number of microtubules persisted on pellicles even after 60 min (Fig. S3). The radii of these asters did not change, consistent with our prediction of stationary asters. Thus, the pellicle experiments confirmed our main experimental result of small, stationary asters and that the nature of transition is consistent with the existence of a gap velocity.

DISCUSSION

An Autocatalytic Model of Aster Growth

It has not been clear whether the standard model of aster growth can explain the morphology of asters observed in all animal cells, including those of extreme size (Mitchison et al., 2015). To resolve this question, we constructed a biophysical framework that incorporates microtubule polymerization dynamics and autocatalytic nucleation. Numerical simulations and analytical solutions (Fig. 2 and 3) recapitulated both stationary and continuously growing asters in a parameter-dependent manner. Interestingly, the explosive transition from "growth" to "no growth" was predicted to involve a finite growth velocity, which we confirmed in biochemical experiments (Fig. 4). Our model exhibits these behaviors with experimentally determined parameter values

(Table 1 and Fig. 2) and offers a new understanding for how asters grow to span large cytoplasms.

Our model has important caveats in both assumptions and parameter estimation. The two-state model of plus end dynamics neglects subunit level fluctuations (Gardner et al., 2011; Needleman et al., 2010), which are important for individual microtubule but not for large microtubule networks. We also neglect outward sliding of microtubules, which is not required for aster growth, but can accelerate it in vivo (Ishihara et al., 2014a; Wühr et al., 2010). Most importantly, we assume that nucleation is stimulated by growing plus ends, which has little experimental support. However, lacking structural information on how the most promising candidate for nucleation, the gamma-tubulin ring complex, is activated (Kollman et al., 2011) or targeted to microtubules, we argue that our model is an useful starting point that captures the qualitative effect of autocatalytic nucleation in a mathematically tractable manner.

Phase Diagram for Aster Growth

How do large cells control aster size during rapid divisions? We summarize our theoretical findings with a phase diagram for aster growth in Fig. 5. Small mitotic asters are represented by stationary asters found in the regime of bounded polymerization dynamics $J < 0$ and low nucleation rates. These model parameters must change as cells transition from mitosis to interphase to produce large growing asters. Polymerization dynamics becomes more favorable of elongation during interphase (Belmont et al., 1990; Verde et al., 1992), and an increase in the nucleation rate of new microtubules is also possible.

According to the standard model, increasing J to a positive value with no nucleation leads to asters in the "individual growth" regime. A previous study suggested the interphase cytoplasm is in the unbounded polymerization dynamics $J > 0$ (Verde et al., 1992), but our measurements of parameters used to calculate J differ greatly (Table 1). Individual growth regime is also inconsistent with the steady-state density of microtubules at the periphery of large asters in both fish and frog embryos (Ishihara et al., 2014a; Wühr et al., 2008, 2010). Experiments in egg extracts further confirm the addition of new microtubules during aster growth (Ishihara et al., 2014a) contrary to

the predictions of the standard model. Furthermore, the presence of a high density of growing plus ends in the interior of growing asters in egg extract suggests that microtubules must be short compared to aster radius, and mean growth velocity must be negative, at least in the aster interior (Ishihara et al., 2014a). As noted above, mean growth velocity could be different at the periphery vs. in the interior if negative feedback alters polymerization dynamics.

By constructing a model that incorporates autocatalytic nucleation $r > 0$, we discovered a new regime, in which continuous aster growth is supported even when microtubules shrink on average ($J < 0$). We call this the "collective growth" regime because individual microtubules are much shorter (estimated mean length of 9-30 μm, Table 1) than the aster radius (hundreds of microns). Predictions of this model are fully confirmed by the biochemical perturbation of the microtubule catastrophe factor with MCAK-Q710, and the inferred rate of nucleation (Table 1) is comparable to previous measurements in meiotic extract (Clausen and Ribbeck, 2007; Petry et al., 2013).

Collective Growth of Cytoskeletal Structures

Our theory allows for independent regulation of aster growth rate and microtubule density through the control of the nucleation rate and microtubule polymerization. Thus, cells have a lot of flexibility in optimizing aster properties and behavior. In particular, the existence of a gap velocity results in switch-like transition from quiescence to rapid growth and allows cells to drastically alter aster morphology with a small change of parameters. Importantly, the rapid growth does not require high microtubule density inside asters, which can be tuned by small changes in the nucleation rate.

Collective growth produces a meshwork of short microtubules with potentially desirable properties. First, the network is robust to microtubule severing or the spontaneous detachment from the centrosome. Second, the network can span arbitrary large distances yet disassemble rapidly upon mitotic entry. Third, the structure, and therefore the mechanical properties, of the network do not depend on the distance from the centrosome. As a speculation, the physical interconnection of the microtubules may facilitate the transduction of mechanical forces across the cell in a way unattainable in

the radial array predicted by the standard model (Tanimoto et al., 2016; Wühr et al., 2010).

The regime of collective growth parallels the assembly of other large cellular structures from short, interacting filaments and is particularly reminiscent of how meiosis-II spindles self-assemble (Brugues and Needleman, 2014; Brugues et al., 2012; Burbank et al., 2007). Due to such dynamic architecture, spindles are known to have unique physical properties such as self-repair, fusion (Gatlin et al., 2009) and scaling (Good et al., 2013; Hazel et al., 2013; Wühr et al., 2008), which could allow for greater robustness and evolvability (Kirschner and Gerhart, 1998). Perhaps, collective growth is one of the most reliable ways for a cell to assemble cytoskeletal structures that exceed the typical length scales of individual filaments.

MATERIALS AND METHODS

Numerical Simulations

We implemented a finite difference method with fixed time steps to numerically solve the continuum model (Eq. (1)). Forward Euler's discretization scheme was used except exact solutions of advection equations was used to account for the gradient terms. Specifically, the plus end positions were simply shifted by $+v_g\delta t$ for growing microtubules and by $-v_s\delta t$ for shrinking microtubules. Nucleation added new growing microtubules of zero length at a position-dependent rate given by $Q(x)$. The algorithm was implemented using MATLAB (Mathworks).

Analytical Solution

We linearized Eq. (1) for small C_g and solved it using Laplace transforms in both space and time. The inverse Laplace transform was evaluated using the saddle point method (Bender and Orszag, 1999), and we found that the expansion velocity is given by

$$V = \frac{v_g(v_g f_{res} - v_s f_{cat})^2}{\left(\begin{array}{r} v_g(v_g f_{res} - v_s f_{cat})(f_{res} + f_{cat}) + (v_g + v_s)(v_g f_{res} + v_s f_{cat})r \\ -2(v_g + v_s)\sqrt{v_g f_{cat} f_{res} r(v_g f_{res} - v_s f_{cat} + v_s r)} \end{array}\right)}$$

The details of this calculation are summarized in the Supporting Text (SI).

Aster Growth Velocity Measurements

Interphase microtubule asters were reconstituted in *Xenopus* egg extract as described previously with use of p150-CC1 to inhibit dynein mediated microtubule sliding (Field et al., 2014; Ishihara et al., 2014a). Fluorescence microscopy was performed on a Nikon 90i upright microscope equipped with a Prior Proscan II motorized stage. EB1-mApple was imaged every 2 min with a 10x Plan Apo 0.45 N.A. or a 20x Plan Apo 0.75 N.A. objective. For the analysis of the aster growth front, a linear region originating from the center of asters was chosen (Fig. S2). The fluorescence intensity profile was passed through a low pass filter and the half-max position, corresponding to the aster edge, was determined manually. The analysis was assisted by scripts written in ImageJ and MATLAB (Mathworks). Univariate scatter plots were generated with an Excel template from (Weissgerber et al., 2015) available at www.ctspedia.org/do/view/CTSpedia/TemplateTesting. In some experiments, MCAK or MCAK-Q710-GFP (Moore and Wordeman, 2004) proteins were added to the reactions. Protein A Dynabeads coated with anti-Aurora kinase A antibody (Tsai and Zheng, 2005) or *Tetrahymena* pellicles were used as microtubule nucleating sites.

Estimation of the Catastrophe Rate

Interphase asters were assembled as described above. Catastrophe rates were estimated from time lapse images of EB1 comets that localize to growing plus ends (Tirnauer et al., 2004). Spinning disc confocal microscopy was performed on a Nikon Ti motorized inverted microscope equipped with Perfect Focus, a Prior Proscan II motorized stage, Yokagawa CSU-X1 spinning disk confocal with Spectral Applied Research Aurora Borealis modification, Spectral Applied Research LMM-5 laser merge module with AOTF controlled solid state lasers: 488nm (100mW), 561nm (100mW), and Hamamatsu ORCA-AG cooled CCD camera. EB1-GFP and EB1-mApple were purified as in (Petry et al., 2011), used at a final concentration of 100 nM, and imaged every 2 sec with a 60x Plan Apo 1.40 N.A objective with 2x2 binning. EB1 tracks were analyzed with PlusTipTracker (Applegate et al., 2011). The distributions of EB1 track

durations were fitted to an exponential function to estimate the catastrophe rate.

Author Contributions

KI and KK developed and analyzed the model. KI performed the experiments and analyzed the data. KI, KK, and TM designed the research and wrote the manuscript.

Acknowledgments

We thank the members of Mitchison and Korolev groups for helpful discussion. This work was supported by NIH grant GM39565 and by MBL summer fellowships. The computations in this paper were run on the Odyssey cluster supported by the FAS Division of Science, Research Computing Group at Harvard University. We thank Nikon Imaging Center at Harvard Medical School, and Nikon Inc. at Marine Biological Laboratory for microscopy support. We thank Ryoma Ohi for providing MCAK and expert advice. We thank Linda Wordeman for providing MCAK-Q710-GFP and expert advice. KK was supported by a start up fund from Boston University. KI was supported by the Honjo International Scholarship Foundation.

References

Akhmanova, A. and Steinmetz, M. O. (2015). Control of microtubule organization and dynamics: two ends in the limelight. *Nature reviews Molecular cell biology*.

Applegate, K. T., Besson, S., Matov, A., Bagonis, M. H., Jaqaman, K., and Danuser, G. (2011). plusTipTracker: Quantitative image analysis software for the measurement of microtubule dynamics. *Journal of structural biology*, 176(2):168–184.

Belmont, L. D., Hyman, A. A., Sawin, K. E., and Mitchison, T. J. (1990). Real-time visualization of cell cycle-dependent changes in microtubule dynamics in cytoplasmic extracts. *Cell*, 62(3):579–589.

Bender, C. M. and Orszag, S. A. (1999). *Advanced Mathematical Methods for Scientists and Engineers I*. Asymptotic Methods and Perturbation Theory. Springer Science & Business Media.

Brinkley, B. R. (1985). Microtubule organizing centers. *Annual review of cell biology*, 1:145–172.

Brugues, J. and Needleman, D. (2014). Physical basis of spindle self-organization. *Proceedings of the National Academy of Sciences of the United States of America*.

Brugues, J., Nuzzo, V., Mazur, E., and Needleman, D. J. (2012). Nucleation and Transport Organize Microtubules in Metaphase Spindles. *Cell*, 149(3):554–564.

Burbank, K. S., Mitchison, T. J., and Fisher, D. S. (2007). Slide-and-cluster models for spindle assembly. *Current biology : CB*, 17(16):1373–1383.

Chang, J. B. and Ferrell, J. E. (2013). Mitotic trigger waves and the spatial coordination of the Xenopus cell cycle. *Nature*, 500(7464):603–607.

Clausen, T. and Ribbeck, K. (2007). Self-organization of anastral spindles by synergy of dynamic instability, autocatalytic microtubule production, and a spatial signaling gradient. *PloS one*, 2(2):e244.

Dogterom, M. and Leibler, S. (1993). Physical aspects of the growth and regulation of microtubule structures. *Physical review letters*, 70(9):1347–1350.

Efimov, A., Kharitonov, A., Efimova, N., Loncarek, J., Miller, P. M., Andreyeva, N., Gleeson, P., Galjart, N., Maia, A. R. R., McLeod, I. X., Yates, J. R., Maiato, H., Khodjakov, A., Akhmanova, A., and Kaverina, I. (2007). Asymmetric CLASP-dependent nucleation of noncentrosomal microtubules at the trans-Golgi network. *Developmental Cell*, 12(6):917–930.

Etienne-Manneville, S. (2013). Microtubules in Cell Migration. *Annual Review of Cell and Developmental Biology*, 29(1):471–499.

Field, C. M., Groen, A. C., Nguyen, P. A., and Mitchison, T. J. (2015). Spindle-to-cortex communication in cleaving, polyspermic Xenopus eggs. *Molecular biology of the cell*, 26(20):3628–3640.

Field, C. M., Nguyen, P. A., Ishihara, K., Groen, A. C., and Mitchison, T. J. (2014). Xenopus egg cytoplasm with intact actin. *Methods in enzymology*, 540:399–415.

Gardner, M. K., Charlebois, B. D., Jánosi, I. M., Howard, J., Hunt, A. J., and Odde, D. J. (2011). Rapid microtubule self-assembly kinetics. *Cell*, 146(4):582–592.

Gatlin, J. C., Matov, A., Groen, A. C., Needleman, D. J., Maresca, T. J., Danuser, G., Mitchison, T. J., and Salmon, E. D. (2009). Spindle fusion requires dynein-mediated sliding of oppositely oriented microtubules. *Current biology : CB*, 19(4):287–296.

Good, M. C., Vahey, M. D., Skandarajah, A., Fletcher, D. A., and Heald, R. (2013). Cytoplasmic volume modulates spindle size during embryogenesis. *Science (New York, NY)*, 342(6160):856–860.

Grigoriev, I., Gouveia, S. M., Van der Vaart, B., and Demmers, J. (2008). STIM1 Is a MT-Plus-End-Tracking Protein Involved in Remodeling of the ER. *Current Biology*.

Grill, S. W. and Hyman, A. A. (2005). Spindle positioning by cortical pulling forces. *Developmental Cell*, 8(4):461–465.

Hallatschek, O. and Korolev, K. S. (2009). Fisher Waves in the Strong Noise Limit. *Physical review letters*, 103(10):108103.

Hazel, J., Krutkramelis, K., Mooney, P., Tomschik, M., Gerow, K., Oakey, J., and Gatlin, J. C. (2013). Changes in cytoplasmic volume are sufficient to drive spindle scaling. *Science (New York, NY)*, 342(6160):853–856.

Ishihara, K., Nguyen, P. A., Groen, A. C., Field, C. M., and Mitchison, T. J. (2014a). Microtubule nucleation remote from centrosomes may explain how asters span large cells. *Proceedings of the National Academy of Sciences of the United States of America*, 111(50):17715–17722.

Ishihara, K., Nguyen, P. A., Wühr, M., Groen, A. C., Field, C. M., and Mitchison, T. J. (2014b). Organization of early frog embryos by chemical waves emanating from centrosomes. *Philosophical Transactions of the Royal Society B: Biological Sciences*, 369(1650).

Keating, T. J. and Borisy, G. G. (1999). Centrosomal and non-centrosomal microtubules. *Biology of the Cell*, 91(4-5):321–329.

Keating, T. J., Peloquin, J. G., Rodionov, V. I., Momcilovic, D., and Borisy, G. G. (1997). Microtubule release from the centrosome. *Proceedings of the National Academy of Sciences of the United States of America*, 94(10):5078–5083.

Kinoshita, K., Arnal, I., Desai, A., Drechsel, D. N., and Hyman, A. A. (2001). Reconstitution of physiological microtubule dynamics using purified components. *Science (New York, NY)*, 294(5545):1340–1343.

Kirschner, M. and Gerhart, J. (1998). Evolvability. *Proceedings of the National Academy of Sciences of the United States of America*, 95(15):8420–8427.

Kollman, J. M., Merdes, A., Mourey, L., and Agard, D. A. (2011). Microtubule nucleation by γ-tubulin complexes. *Nature reviews Molecular cell biology*, 12(11):709–721.

Méndez, V., Fedotov, S., Campos, D., and Horsthemke, W. (2007). Biased random walks and propagation failure. *Physical review E, Statistical, nonlinear, and soft matter physics*, 75(1 Pt 1):011118.

Mitchison, T. and Kirschner, M. (1984). Dynamic instability of microtubule growth. *Nature*.

Mitchison, T. J., Ishihara, K., Nguyen, P., and Wühr, M. (2015). Size Scaling of Microtubule Assemblies in Early Xenopus Embryos. *Cold Spring Harbor perspectives in biology*.

Moore, A. and Wordeman, L. (2004). C-terminus of mitotic centromere-associated kinesin (MCAK) inhibits its lattice-stimulated ATPase activity. *The Biochemical journal*, 383(Pt 2):227–235.

Needleman, D. J., Groen, A., Ohi, R., Maresca, T., Mirny, L., and Mitchison, T. (2010). Fast microtubule dynamics in meiotic spindles measured by single molecule imaging: evidence that the spindle environment does not stabilize microtubules. *Molecular biology of the cell*, 21(2):323–333.

Neumüller, R. A. and Knoblich, J. A. (2009). Dividing cellular asymmetry: asymmetric cell division and its implications for stem cells and cancer. *Genes & Development*, 23(23):2675–2699.

Nguyen, P. A., Groen, A. C., Loose, M., Ishihara, K., Wühr, M., Field, C. M., and Mitchison, T. J. (2014). Spatial organization of cytokinesis signaling reconstituted in a cell-free system. *Science (New York, NY)*, 346(6206):244–247.

Petry, S., Groen, A. C., Ishihara, K., Mitchison, T. J., and Vale, R. D. (2013). Branching microtubule nucleation in Xenopus egg extracts mediated by augmin and TPX2. *Cell*, 152(4):768–777.

Petry, S., Pugieux, C., Nédélec, F. J., and Vale, R. D. (2011). Augmin promotes meiotic spindle formation and bipolarity in Xenopus egg extracts. *Proceedings of the National Academy of Sciences of the United States of America*, 108(35):14473–14478.

Roll-Mecak, A. and McNally, F. J. (2010). Microtubule-severing enzymes. *Current opinion in cell biology*, 22(1):96–103.

Tanimoto, H., Kimura, A., and Minc, N. (2016). Shape-motion relationships of centering microtubule asters. *The Journal of cell biology*, 212(7):777–787.

Tirnauer, J. S., Salmon, E. D., and Mitchison, T. J. (2004). Microtubule plus-end dynamics in Xenopus egg extract spindles. *Molecular biology of the cell*, 15(4):1776–1784.

Tsai, M.-Y. and Zheng, Y. (2005). Aurora A kinase-coated beads function as microtubule-organizing centers and enhance RanGTP-induced spindle assembly. *Current biology : CB*, 15(23):2156–2163.

van Saarloos, W. (2003). Front propagation into unstable states. *Physics Reports*, 386(2-6):29–222.

Verde, F., Dogterom, M., Stelzer, E., Karsenti, E., and Leibler, S. (1992). Control of microtubule dynamics and length by cyclin A- and cyclin B-dependent kinases in Xenopus egg extracts. *The Journal of cell biology*, 118(5):1097–1108.

Walczak, C. E., Mitchison, T. J., and Desai, A. (1996). XKCM1: a Xenopus kinesin-related protein that regulates microtubule dynamics during mitotic spindle assembly. *Cell*, 84(1):37–47.

Wang, S., Romano, F. B., Field, C. M., Mitchison, T. J., and Rapoport, T. A. (2013). Multiple mechanisms determine ER network morphology during the cell cycle in Xenopus egg extracts. *The Journal of cell biology*, 203(5):801–814.

Waterman-Storer, C., Duey, D. Y., Weber, K. L., Keech, J., Cheney, R. E., Salmon, E. D., and Bement, W. M. (2000). Microtubules remodel actomyosin networks in Xenopus egg extracts via two mechanisms of F-actin transport. *The Journal of cell biology*, 150(2):361–376.

Waterman-Storer, C. M. and Salmon, E. D. (1998). Endoplasmic reticulum membrane tubules are distributed by microtubules in living cells using three distinct mechanisms. *Current biology : CB*, 8(14):798–806.

Weissgerber, T. L., Milic, N. M., Winham, S. J., and Garovic, V. D. (2015). Beyond bar and line graphs: time for a new data presentation paradigm. *PLoS Biology*, 13(4):e1002128.

Wilson, E. B. (1896). *The Cell in development and inheritance*. Macmillan, New York.

Wühr, M., Chen, Y., Dumont, S., Groen, A. C., Needleman, D. J., Salic, A., and Mitchison, T. J. (2008). Evidence for an upper limit to mitotic spindle length. *Current biology : CB*, 18(16):1256–1261.

Wühr, M., Dumont, S., Groen, A. C., Needleman, D. J., and Mitchison, T. J. (2009). How does a millimeter-sized cell find its center? *Cell cycle (Georgetown, Tex)*, 8(8):1115–1121.

Wühr, M., Tan, E. S., Parker, S. K., Detrich, H. W., and Mitchison, T. J. (2010). A model for cleavage plane determination in early amphibian and fish embryos. *Current biology : CB*, 20(22):2040–2045.

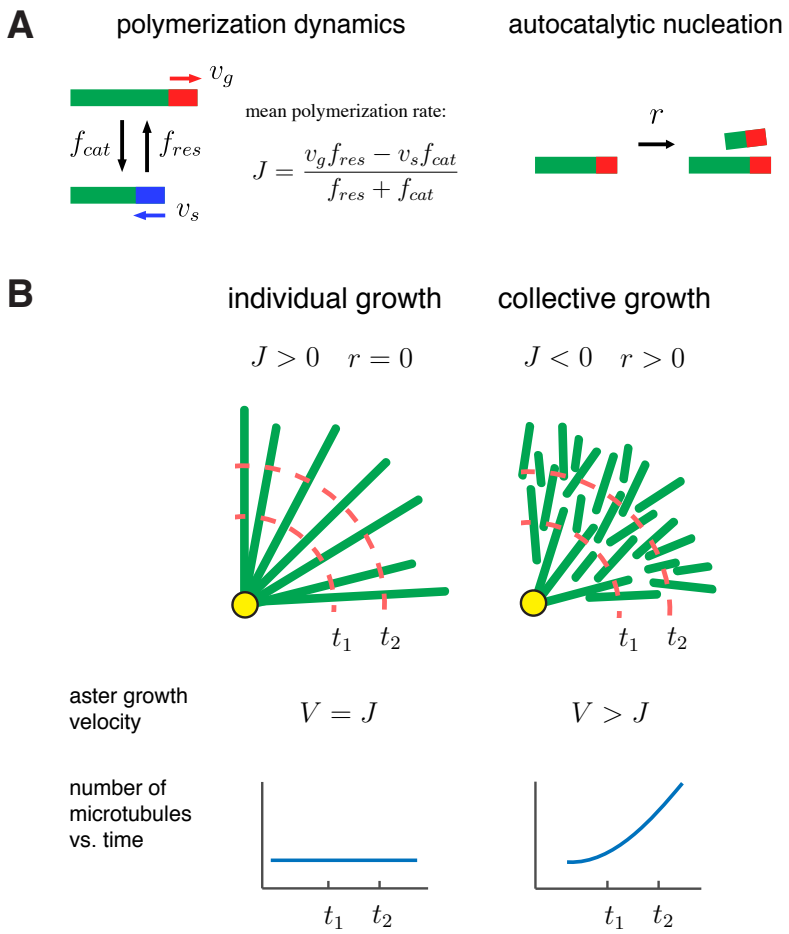

Figure 1. A biophysical model for the collective growth of microtubule asters. (A) We propose that asters grow via two microscopic processes: polymerization and nucleation. Individual microtubules follow the standard dynamic instability with a growing sate with polymerization rate v_g and a shrinking state with depolymerization rate v_s. Transitions between the states occur at rates f_{cat} and f_{res}. New microtubules are added at a rate r via a nucleation at pre-existing plus ends in the growing state. (B) The contrast between individual and collective growth of asters. In the standard model of "individual growth", asters expand only via a net polymerization from the centrosome (yellow) without the nucleation of new microtubules. This model predicts that the rate of aster growth equals the mean polymerization rate $V = J$, the number of microtubules is constant, and their density decreases away from the centrosomes. In contrast, the microtubule density is constant in the collective growth model, and the number of microtubules increases. Autocatalytic nucleation makes asters grow faster than the net polymerization rate J and can sustain growth even when individual microtubules depolymerize on average $J < 0$.

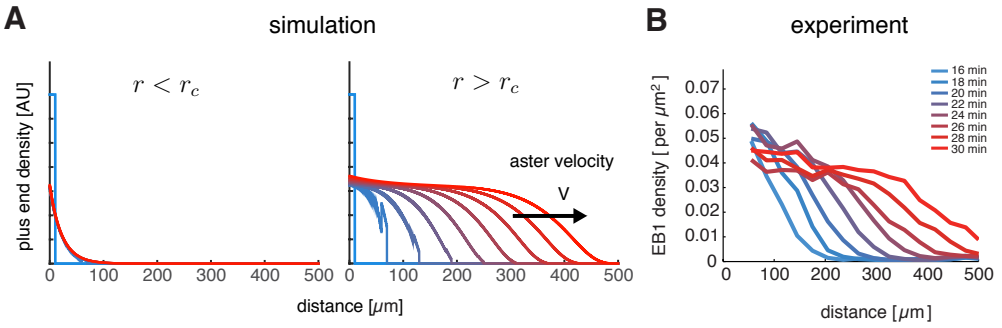

Figure 2. Our model captures key features of large aster growth. (A) Time evolution of growing plus end density predicted by our model, which we solved via numerical simulations in 1D geometry. In the stationary regime, the microtubule population remained near the centrosome $v_g = 30$, $v_s = 40$, $f_{cat} = 3$, $f_{res} = 1$, and $r = 1.0$ (left). In contrast, outward expansion of the microtubule population was observed when the nucleation rate was increased to $r = 2.5$, above the critical nucleation rate r_c (right). For both simulations, microtubules are in the bounded regime $J < 0$. (B) Experimental measurements confirm that asters expand at a constant rate with time-invariant profiles of the plus end density, as predicted by our model. The plus end densities were estimated as EB1 comet density during aster growth as previously described. Reprinted with permission from (Ishihara et al., 2014a).

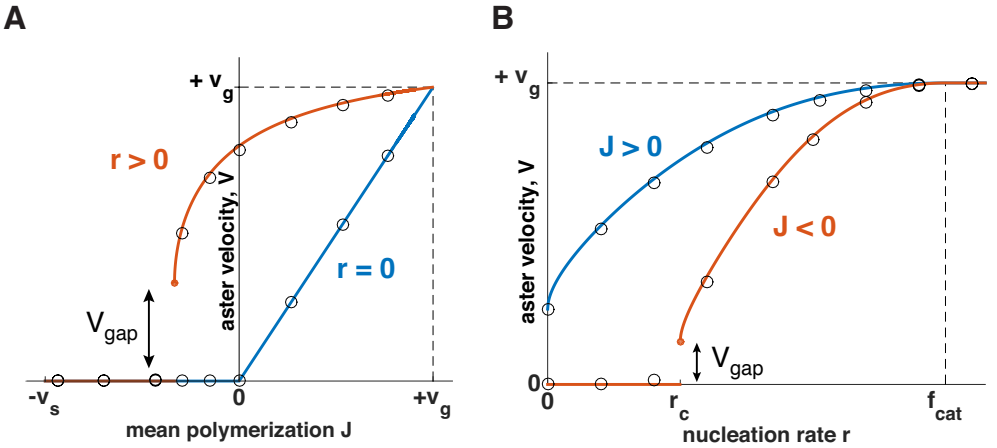

Figure 3. Explosive transition from stationary to growing asters and other theoretical predictions. Analytical solution (lines) and numerical simulations (dots) predict that asters either remain stationary or expand at a constant velocity, which increases with the net polymerization rate J (A) and nucleation rate r (B). The transition to a growing state is accompanied by finite jump in the expansion velocity labeled as V_{gap}. (A) The behavior in the standard model ($r = 0$) is shown in blue and our model ($r = 1.5$) in red. Note that aster growth commences at $J < 0$ in the presence of nucleation and occurs at a minimal velocity V_{gap}. Although spatial growth can occur for both $J > 0$ and $J < 0$ the properties of the resulting asters could be very different (see SI). Here, $v_g = 30, v_s = 30, f_{cat} = 3$. (B) If $J < 0$, critical nucleation r_c is required to commence aster growth. Blue line corresponds to $J > 0 (v_g = 30, v_s = 15, f_{cat} = 3, f_{res} = 3)$ and red line to $J < 0 (v_g = 30, v_s = 15, f_{cat} = 3, f_{res} = 1)$. See Materials and Methods and SI for the details of the analytical solution and numerical simulations.

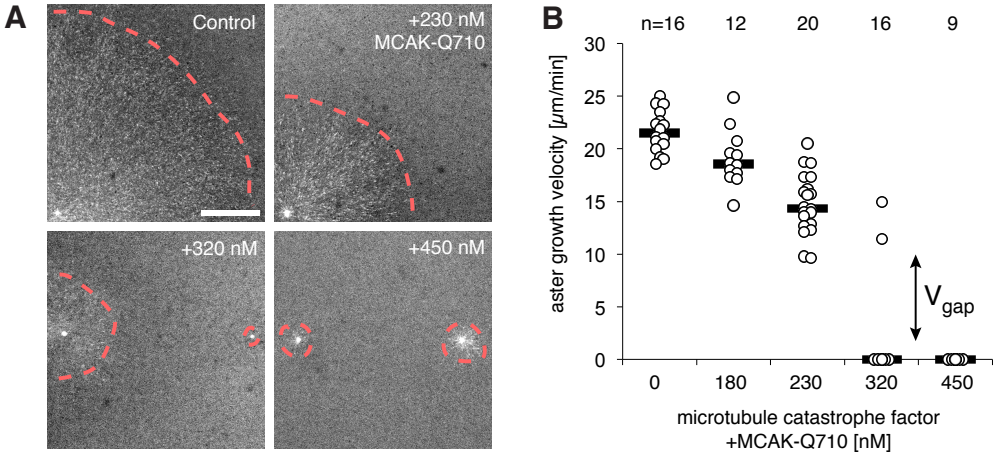

Figure 4. Titration of MCAK-Q710 slows then arrests aster growth through a discontinuous transition. (A) Addition of catastrophe promoting factor MCAK-Q710 results in smaller interphase asters reconstituted in *Xenopus* egg extract. Images were obtained 20 minutes post initiation with the plus end marker EB1-mApple. Dotted lines indicate the approximate outline of asters. (B) Aster growth velocity decreases with MCAK-Q710 concentration and then abruptly vanishes as predicted by the model. Note a clear gap in the values of the observed velocities and bimodality near the transition, which support the existence of V_{gap}. Quantification methods are described in methods and Fig. S2.

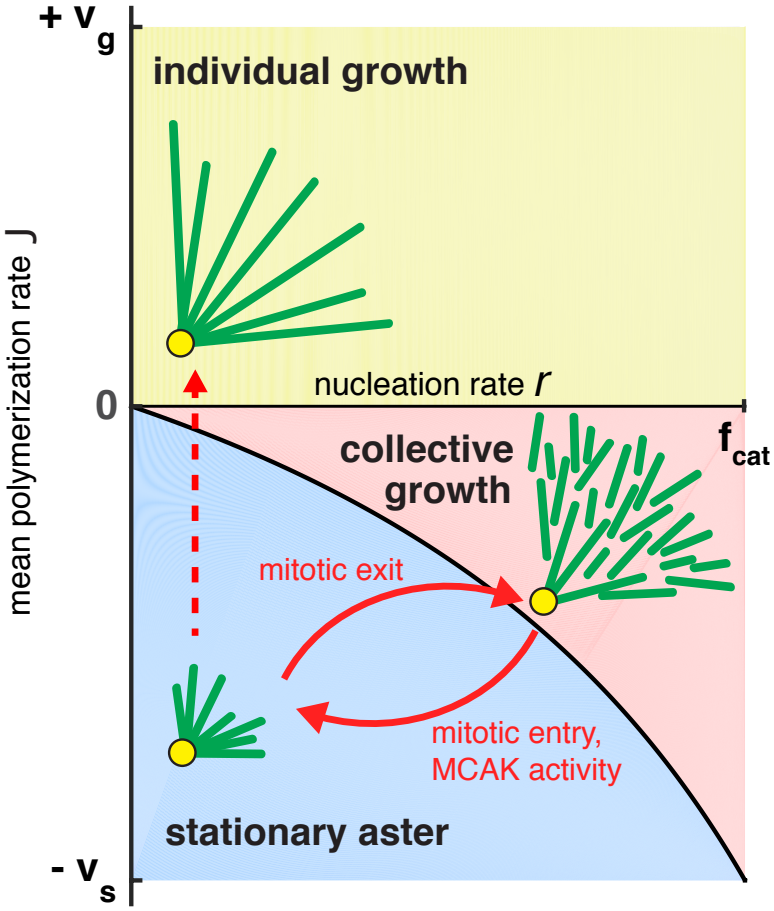

Figure 5. Phase diagram for aster growth. Aster morphology is determined by the balance of polymerization dynamics and autocatalytic nucleation. Small, stationary asters, as observed during mitosis, occur at low nucleation r and net depolymerization of individual microtubules ($J < 0$). Net polymerization ($J > 0$) without nucleation ($r = 0$) produces asters that expand with dilution of microtubule density at the periphery and are thus inconsistent with experimental observations. The addition of nucleation to the individual growth regime changes these dynamics only marginally (yellow region); see SI. Alternatively, the transition from stationary to growing asters can be achieved by increasing the nucleation rate, r, while keeping J negative. Above the critical nucleation rate r_c starts the regime of collective growth that produces asters composed of relatively short microtubules (red region). Reverse transition recapitulates the results of our experimental perturbation of MCAK activity and mitotic entry (solid arrows). We propose this unified biophysical picture as an explanation for the cell cycle dependent changes of aster morphology *in vivo*.

Quantity	Symbol	Value	Comment
Aster expansion velocity	V	22 μ m/min	Rate of radius increase
Bulk growing plus end density	C_g^{bulk}	0.04 μm^{-2}	Estimate from EB1 comet density
Polymerization rate	v_g	30 μm/min	From tracking growing plus ends and EB1 comets
Depolymerization rate	v_s	42 μm/min	From tracking shrinking plus ends
Catastrophe rate (growing→shrinking)	f_{cat}	3.3 min^{-1}	From EB1 comet lifetimes (see Methods)
Rescue rate (shrinking→growing)	f_{res}	0 - 4.6 min^{-1}	Estimated range assuming bounded dynamics ($J < 0$)
Mean microtubule length	$\langle l \rangle$	9-30 μm	Estimate (see SI) assuming $f_{res} < f_{cat}$
Autocatalytic nucleation rate	r	1.4 - 2.7 min^{-1}	Inferred with aster growth velocity equation (SI)
Carrying capacity of growing plus ends	K	0.4 μm^{-2}	By comparing C_g^{bulk} from experiments to predicted (SI)

Table 1. Model parameters used to describe large aster growth reconstituted in interphase *Xenopus* egg extract (Ishihara et al., 2014a).